Intermetallics 175 (2024) 108540

Contents lists available at ScienceDirect

Intermetallics

journal homepage: www.elsevier.com/locate/intermet

Grain refinement of Inconel 625 during wire-based directed energy deposition additive manufacturing by in-situ added TiB_2 particles: Process development, microstructure evolution and mechanical characterization

Tiago A. Rodrigues [a,**], A. Malfeito [b], Francisco Werley Cipriano Farias [b], V. Duarte [b], João Lopes [b], João da Cruz Payão Filho [c], Julian A. Avila [d], N. Schell [e], Telmo G. Santos [b,f], J.P. Oliveira [g,*]

[a] ISQ, Instituto Soldadura e Qualidade, Taguspark-Oeiras, 2740-120, Porto Salvo, Portugal
[b] UNIDEMI, Departamento de Engenharia Mecânica e Industrial, Faculdade de Ciências e Tecnologia, Universidade NOVA de Lisboa, 2829-516 Caparica, Portugal
[c] Program of Metallurgical and Materials Engineering, Federal University of Rio de Janeiro (UFRJ), CEP 21941-972, Rio de Janeiro RJ, Brazil
[d] São Paulo State University (UNESP), Campus of São João da Boa Vista, Av. Profª Isette Corrêa Fontão, 505, Jardim das Flores, 13876-750, São João da Boa Vista, SP, Brazil
[e] Helmholtz-Zentrum Geesthacht, Institute of Materials Research, Max-Planck-Str. 1, Geesthacht, 21502, Germany
[f] Laboratório Associado de Sistemas Inteligentes, LASI, 4800-058 Guimarães, Portugal
[g] CENIMAT/I3N, Department of Materials Science, NOVA School of Science and Technology, Universidade NOVA de Lisboa, 2829-516 Caparica, Portugal

ARTICLE INFO

Keywords:
Inconel
Titanium diboride
Wire and arc additive manufacturing
Directed energy deposition
Grain refinement
Inoculants
Synchrotron X-ray diffraction

ABSTRACT

In this study, a novel method for enhancing the quality of components fabricated by wire and arc additive manufacturing (WAAM) was developed. This approach employs an innovative mechanism featuring an actuator that dispenses a solution containing refinement particles (TiB_2 inoculants), in conjunction with a soldering flux that vaporizes prior to reaching the electric arc. This leaves the particles to adhere to the welding wire or be carried by the shielding gas. By implementing this device, TiB_2 particles were successfully incorporated into the molten pool during the WAAM process of Inconel 625 at levels of 0.31 and 0.56 wt%. Microstructural analysis reveals a significant reduction in the size of interdendritic segregation regions when TiB_2 particles are introduced. Electron backscatter diffraction analysis further reveals the transformation of columnar grains into equiaxed grains. The average grain area decreased from 1823 μm^2 in the as-built sample to 583 μm^2 in the sample with a TiB_2 content of 0.56 wt%. In addition, an improvement in the Inconel 625 fabricated by WAAM mechanical strength was observed due to the use of TiB_2 inoculants, which was primarily attributed to the effect of the grain size refinement.

1. Introduction

Wire and arc additive manufacturing (WAAM) is a variant within the metal additive manufacturing realm, based on the fundamentals of arc welding, where a wire feedstock material is melted by an electric arc and deposited in a layer-by-layer fashion. According to ISO/ASTM 52900:2021, WAAM belong to the class of directed energy deposition (DED) processes and ASTM F3187-16 referred to WAAM as arc plasma DED [1]. However, considering that the nomenclature WAAM is well established in the scientific community, for a better understanding, the arc plasma DED process will be referred to as WAAM in this study. The key feature of WAAM concerning other DED processes (e.g., laser and electron beam-based) is the high deposition rates (1–10 kg/h) [2], making it more proficient for fabricating medium/large parts. Another crucial characteristic, it is low implementation costs, as the elements used for WAAM are similar to those typically used for arc-based welding (e.g., consumables, power sources, and positioning equipment). Moreover, concerning powder-based AM processes (e.g., blown powder DED), almost total feedstock (solid wire) material is consolidated in WAAM, offering high-efficiency material usage and a significant reduction in raw material cost [3]. All these factors make WAAM more attractive for building medium to large components using alloys where

* Corresponding author.
** Corresponding author.
E-mail addresses: tmrodrigues@isq.pt (T.A. Rodrigues), jp.oliveira@fct.unl.pt (J.P. Oliveira).

https://doi.org/10.1016/j.intermet.2024.108540
Received 10 July 2024; Received in revised form 27 September 2024; Accepted 16 October 2024
Available online 23 October 2024

subtractive technologies are very costly (e.g., Ni- and Ti-based alloys).

Despite the high manufacturing flexibility of WAAM in relation to traditional manufacturing routes (e.g., rolling and forging), the layer-by-layer deposition aspect and the thermal boundary condition in the melting pool typically induced a coarse and texturized microstructure. These aspects are especially significant for non-transformable alloys, such as Inconel 625, which induces anisotropic properties, reduced heat treatment response, and lower corrosion resistance, making Inconel 625 parts fabricated by WAAM unsuitable for critical applications (e.g., oil & gas, aviation, and nuclear industries) [1,2]. In addition, API 20S grain size specification is typically not accomplish [4–6]. Therefore, removing this unwanted microstructure feature is fundamental to be fully embraced by the industry of Inconel 625 parts fabricated by WAAM [7]. Achieving equiaxed grains during fusion-based additive manufacturing can be achieved by controlling the processing parameters and consequently manipulating the temperature gradient (G) and the growth rate (R) of the solid/liquid (S/L) interface [8]. It is well known that columnar to equiaxed grains are favored when R increases and G decreases [9]. In general, WAAM presents lower cooling rates and solidification rates (lower travel speed) compared to other fusion-based AM processes (e.g., laser powder bed fusion). Also, WAAM possesses a higher penetration, i.e., the subsequent layer completely remelted the columnar-to-equiaxed transition zone that occurred in the top surface promoted epitaxial growth (coarse columnar grains) [10]. Additionally, gas metal arc-based WAAM exhibited narrow process parameter window for Ni-based superalloys (e.g., Inconel 625) that ensures a high printability (e.g., stable deposition aspect and absence of lack of fusion and hot cracks) [11]. Thus, inducing a finer and non-oriented microstructure through process parameters control is still a challenge for Ni-based superalloys fabricated by WAAM. In this sense, previous techniques applied to casting and welding were also tested to refine the microstructure of parts fabricated by WAAM, e.g., the introduction of inoculants on the melting pool, cold and hot deformation, vibration, external magnet field stir, use of pulsed current, and forced cooling [12–18]. However, the use of interlayer deformation can restrict the flexibility of WAAM, and vibration can be limited by the part size. Magnetic field stirring and forced cooling have demonstrated lower efficiency due to the intense thermal gradient in the molten pool, and the use of different metal transfer and current modes can be limited for alloys that have a history of weldability problems (e.g., hot cracking). Thus, adding inoculants to the molten pool proves to be an interesting technique for avoiding the typical coarse and oriented microstructure observed in Inconel 625 parts fabricated by WAAM since this technology is independent of alloy type, part size/geometry, and additive manufacturing process.

Effective nucleating particles (inoculants) are one of the most efficient technologies to induce heterogeneous nucleation (grain size refiner) on the melting pool due to the small supercooling required for epitaxial growth. In addition, segregating solute develops a constitutionally supercooled zone that restricts further growth of the primary dendrites and enables neighboring particles to actively form new grains [19]. One of the most important considerations influencing the potency of a particle to be used is its size, where the largest particles have the highest potency for nucleation [20]. Also, the melting point of this particle must be considered, where this must be higher than the maximum temperature of the melting pool [13,19,21]. However, considering the higher temperature of the electric arc (e.g., 7000 K) [22], some particles can also melt, slightly altering the final chemical composition of the printed part.

In this work, titanium diboride (TiB_2) was chosen to be added to the Inconel's molten pool, as this refractory intermetallic compound has a melting point high as 3225 °C [23]. It is also characterized by high hardness, corrosion resistance, and wear resistance. Although TiB_2 has a very high melting point, dissociation can occur upon contact with the liquid Inconel. Assuming that some of the TiB_2 will dissociate, the incorporation of Ti can further enhance the mechanical properties of the solidified material by solid solution strengthening and can also enable the precipitation of γ' (Ni_3Ti) [24]. Furthermore, the addition of B in solid solution can also restrict the lateral growth of the columnar grains (i.e., reduce the grain width) [19]. This was attributed to the large solute rejection to the interdendritic regions, that accumulated between the columnar grains, restricting lateral columnar growth. In the coating industry, nano-TiB_2 has been highly used in concentrations up to 40 wt% with Inconel 625 to create metal matrix composites [25]. The authors stated that the low interface energy between TiB_2 and γ (200–500 mJ/m^2) produces a small contact angle and is good enough to maintain excellent wettability and therefore promote heterogeneous nucleation. In addition, TiB_2 has higher thermal diffusivity (5.98×10^{-6} vs 2.08×10^{-6} m^2 s^{-1}) and higher thermal conductivity (25 vs 11.4 W m^{-1} K^{-1}) than the γ phase indicating that the temperature of the particles will be lower during solidification than the surrounding liquid, providing favorable conditions for heterogeneous nucleation.

Adding inoculants in process that use powder as feedstock material is simple task since the powders (feedstock material and inoculant) can be directly mixed in the feeding system, such as occurred in the laser DED (blown-powder) process. Zhang et al. [26] reported that Inconel 625 powder mixed with TiB_2 particles in a weight ratio of 97.5:2.5 can improve the strength and wear resistance of fabricated parts. The tensile strength was improved from 840 to 1020 MPa and the elongation was increased from 16 to 18 %. Moreover, a substantial hardness increases was observed (from 255 to 347 HV). For WAAM, the techniques to insert refinement particles in the molten pool become more complex due to the typical feedstock material adopted (solid-wire). In addition, the arc pressure and shielding gas can expel inoculants to regions outside the melting pool. To overcome this process limitation, the literature spraying manually the substrate or the last deposited layer with the particles dispersed in an alcohol gel solution [27,28], fixing the inoculants on the part surface, which will migrate to the melting pool. In all these cases, the welding process used was gas tungsten arc welding (GTAW), which can only be automated when used on a 6-axis robot to build complex features, as the wire feedstock has to be fed collinearly with the deposition direction. This study presents a new solution to introduce particles to the melting pool coaxially with the feedstock material, i.e., using the gas metal arc welding (GMAW). To impregnate the feedstock material (wire) with the inoculants, a soldering flux mixture containing the inoculants is injected laterally to the contact tip. The soldering flux evaporates due to the arc heating, leaving only the inoculant particles, which come into contact with the wire and can also be introduced through the arc plasma. In addition to develop the system to introduce inoculants in GMA-based WAAM, the present work also investigate the role of TiB_2 as a grain refiner agent during the WAAM of Inconel 625 parts. Moreover, the relationship between the concentration of TiB_2 and new phases formed, as well as the resulting mechanical properties were investigated by combining electron microscopy, high energy synchrotron X-ray diffraction, mechanical testing, and thermodynamic modeling. In addition, the mechanism for grain size refinement was also presented and discussed.

2. Experimental procedure

2.1. Experimental setup

In this study, a 3-axis movement system was used, in which a customized GMAW welding torch was attached to the moving head. This GMAW welding torch had a custom-built device that introduced the TiB_2 particles coaxially with the feedstock material (solid wire filler metal). By having the particles fed coaxially it allows the deposition of complex geometric features to be printed with WAAM without any design constraints. This device was developed accordingly to the following requirements: i) modularity of the welding torch and the system that feeds the particles; ii) introducing the particles coaxially with the wire, to allow complex geometric features deposition, iii) control the weight percentage of particles in each segment of the layer, independently of the wire feed speed. The customized particle feeder device is schematically presented in Fig. 1.

The solution with the particles is placed inside a container, in this case, a syringe (1). To control particle flow rate, a stepper motor (2) or another type of actuator provides the driving force that is transmitted to the dispenser that contains the particles. A power transmission system (3) of a flexible shaft coupling, lead screw, and a linear rail guide (4) allows fine control of the particles' amount. The actuation mechanism can start and stop the flow of the solution and also change the weight percentage of particles locally in the part. Particles after leaving the dispenser (1) flow inside the connection tubes (5) which are connected to the nozzle in the welding torch module.

The connection tubes (5) previously illustrated in Fig. 1 are then connected to a modified conductive nozzle (11) as shown in Fig. 2. The conductive nozzle (11) enters via a hole made in the torch nozzle (9) and is electrically isolated with a non-conductive sleeve (12). As the solution (flux + particles (13)) reaches the conductive nozzle (11), it is heated up and the flux evaporates, leaving the particles to be fed into the molten pool. The inoculation procedure can occur in two ways, either by adhering to the welding wire (14,15) or by flowing with the shielding gas to the molten pool. The flux used is the commercially available SW21 - soldering flux from Nevex, which evaporates when in contact with a hot surface leaving the particles to adhere to the welding wire or by flowing with the shielding gas.

In these experiments, an ER NiCrMo-3 (Inconel 625) filler metal with 1 mm in diameter, and a Pro MIG 3200 GMAW power source were used. The wire feedstock composition can be found in Table 1. TiB_2 particles with a size ranging from 5 to 8 μm were added using the device previously presented in Fig. 1. An interpass temperature of 150 °C was used and controlled with a pyrometer. The depositions were made using a wire feed speed of 4 m/min, while the travel speed was kept at 250 mm/min, the voltage was set to 19 V, and the current to 73 A. These parameters ensured defect-free parts. Rectangular walls with a dimension of 120 × 50 × 9 mm were deposited on a carbon steel substrate. One control sample (0 % of TiB_2) and two others (TiB_2 concentrations of 0.31 and 0.56 wt%) were deposited to evaluate the impact of the added TiB_2 on the microstructure evolution and resulting mechanical properties.

For the microscopy observations, samples were polished using abrasive papers with grits from 80 to 2000 and polished using a 3 μm diamond suspension before etching. The specimens were electrolytically etched in 10 wt% Chromium trioxides dissolved in distilled water at a potential of 5 V for 20 s. Microstructural examinations were carried out by a SU3800 Hitachi scanning electron microscope (SEM) after electrolytic etching. An FEI Quanta FEG – Inspect-F50 SEM equipped with an electron backscatter diffraction (EBSD) camera was used for the EBSD measurements.

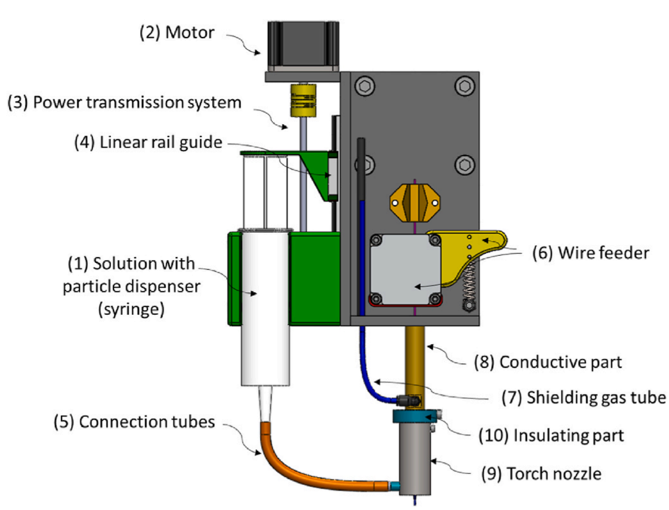

Fig. 1. Illustration of each component in the tailored welding/WAAM torch.

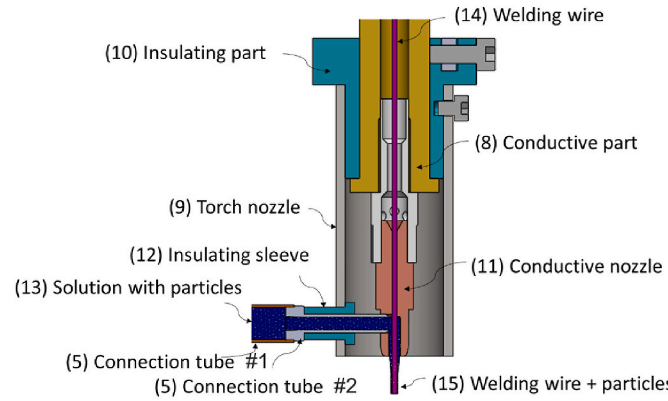

Fig. 2. Section view of the customized welding torch.

Synchrotron X-ray diffraction measurements were performed at the High Energy Materials Science beamline at PETRA III, DESY (Hamburg, Germany) with a beam energy of 87.1 keV (0.14235 Å). A 2D PerkinElmer detector with a pixel size of 200 μm was used to capture the Debye-Scherrer diffraction rings. These were then integrated along the full azimuthal angle (ϕ) using freely available Fit2D software [29] to obtain conventional (Intensity vs. d-spacing) diffraction patterns. The beam size was 1 × 1 mm and LaB_6 calibrant powder was used to estimate the instrumental peak broadening associated with the beamline, and the exposure time was set to 5 s.

The effects of the TiB_2 on mechanical properties were evaluated via compression and hardness testing. For compression testing, two specimens were removed both in the vertical and horizontal directions of each sample. The specimens were manufactured in compliance with ASTM's E9-09 [30] standard, using a length to diameter ratio of 2. Thus, specimens measuring 6 mm in length and 3 mm in diameter were used. The compression testing experiments were carried out using a displacement speed of 1 mm/min. Compression tests were performed on an Autograph Shimadzu machine model AG500Kng equipped with a Shimadzu load cell SFL-50kN AG. It is worth mentioning that the specimens did not fracture during compression tests, reinforcing the ductile characteristics of the Inconel 625 fabricated by WAAM.

Hardness measurements were performed using a Mitutoyo HM-112 Hardness Testing Machine, under a load of 1 N, for 10 s across the sample's total height. The distance between consecutive indentations was set to 250 μm.

2.2. Finite element model of the deposition

A numerical model for the thermal cycles experienced by the Inconel 625 WAAM single-bead multi-layers wall was developed using the commercial ESI *SYSWELD* finite element software to estimate the weld pool temperature and the possible melting of the TiB_2 particles. The model was validated via thermocouples type-K placed on the substrate (5 and 10 mm away from the first layer edge). The model used the geometrical dimensions of a single-bead 10-layer wall and the deposition paraments. To simulate the heat source, the double ellipsoidal of Goldak et al. [31] was used. The heat source dimensions were set via measurement of the final cross-section dimensions. A LabVIEW design program was designed to measure both current and Voltage during depositions to calculate the average arc power. For the current measurements, an open-loop LEM HTA 1000-S current transducer was used with a sampling rate of 10 kHz. The material physical properties (density, specific heat, and thermal conductivity) required for the numerical model were obtained from the ESI *SYSWELD* database. The numerical simulations were performed according to the work of Farias et al. [14]. The entire simulation procedure followed the ISO 18166 standard

Table 1
Chemical composition of the wire feedstock used in this work (wt.%).

Alloy (AWS classification)	C	Mn	Si	Nb	Ti	Al	V	Ni	Cr	Mo	Cu	Fe
Inconel 625 (ER NiCrMo-3)	0.1	0.5	0.5	3.5	0.4	0.4	–	Bal.	21.5	9	0.5	5

recommendations. For details about the model, meshing procedure, formulation, and validation, see Supplementary Material.

3. Results and discussion

3.1. Microscopic characterization

Fig. 3 shows the SEM images taken in the middle of each sample, both in a non-remelted/re-heated area and in a remelted region of the walls. In the as-built Inconel 625 samples, the non-remelted area (refer to Fig. 3 a) presents the typical columnar dendrites with clear secondary dendritic arms caused as a result of the relatively lower cooling rates during solidification, as typical of WAAM. Also, large segregation in the inter-dendritic regions is visible (insert in Fig. 3 a1). The remelted area of the as-built sample (Fig. 3 b) presents columnar dendrites without secondary arms due to higher temperature gradients, as this is the first region of a layer that solidifies. Fig. 3 c) and d) depict the microstructure in the non-remelted and remelted regions in the sample built with 0.31 wt% TiB_2, respectively. The non-remelted and remelted regions also exhibit columnar dendrites with secondary arms and dendrites without secondary arms, respectively. Finally, when the content of TiB_2 increased to 0.56 wt%, the non-remelted region solidified as equiaxed dendrites, but in the remelted area the columnar dendrites are still present. As seen in inserts a1, c1, and e1 in Fig. 3, corresponding to higher magnifications SEM images, upon the introduction of the TiB_2 particles the large segregation regions disappeared from the interdendritic spaces. The inserts in the micrographs depict both a decrease in the Nb-rich Laves phase size and the maintenance of Nb and Ti complex carbides/nitrides in the microstructure. Avoiding the long continuous Laves phase is beneficial as it improves the hot cracking resistance of Inconel [32] and material ductility [33].

Fig. 4 shows the Scheil solidification curve calculations for both Inconel 625 and Inconel 625 with additions of Ti and B, considering a complete dissolution of the 0.56 wt% TiB_2. It is perceived that the solidification temperature range of Inconel 625 is 363 °C, but with additions of Ti and B, the range is reduced to 257 °C. This smaller solidification temperature range will be a benefit in avoiding solidification cracking that can develop in the final stages of solidification. In the sequence of TiB_2-free Inconel 625, Laves phase is formed within the 964–980 °C temperature range, but in the modified alloy the solidus temperature is 1050 °C, and Laves phase does not form. These results indicated that the possible particle dissolution/melting during the process will not induce deleterious effects or reduce the weldability/printability of the alloy.

The reduction in the size of Laves phase and segregated regions is explained by the increased nucleation rate that TiB_2 particles provide ahead of the S/L interface, which will provide less time for the solute to be rejected to interdendritic regions. Besides, as proved by thermodynamic simulations, changes in the composition due to the dissolution of TiB_2 particles can also be beneficial in avoiding the formation of eutectic phases, such as Laves, while reducing the solidification temperature range. Also, the formation of M_3B_2 (predicted in the Scheil solidification

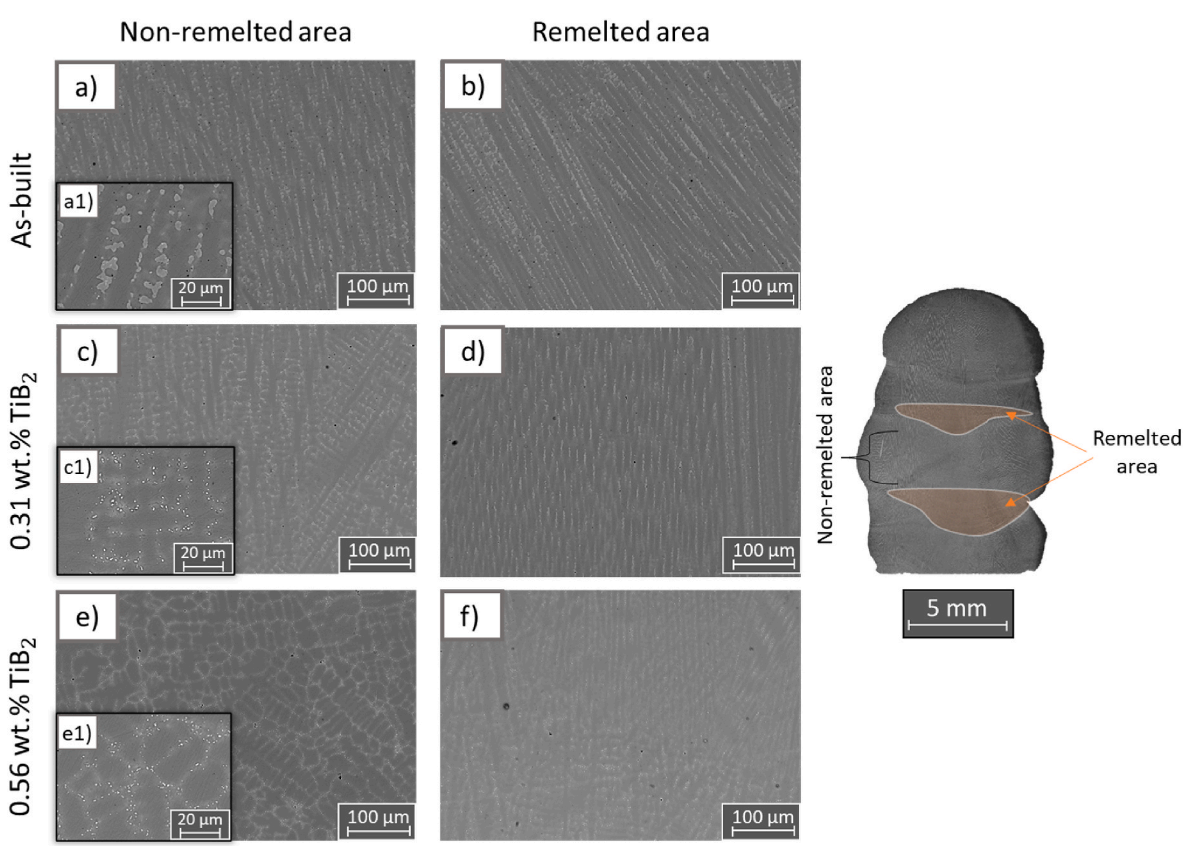

Fig. 3. – SEM images taken from the non-remelted and remelted regions of samples: (a), (b) As-built; (c) (d) Inconel 625 with 0.31 wt% TiB_2; (e) (f) Inconel 625 with 0.56 wt% TiB_2. Inserts a1, c1, and e1 correspond to higher magnification SEM images.

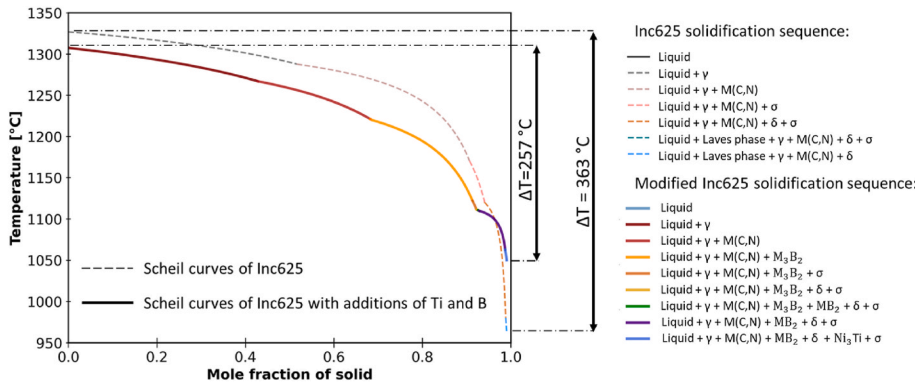

Fig. 4. ThermoCalc Scheil-Gulliver calculations for the Inconel 625, and modified Inconel 625 considering a complete dissolution of TiB_2 in the matrix.

simulation) can reduce the Mo and Nb concentration in the remaining liquid (interdendritic) [34,35], which can also reduce the content of Laves in the inoculated condition.

Since the addition of 0.56 wt % TiB_2 resulted in significant solidification microstructure changes (compared to the 0.31 wt % TiB_2 containing sample), the focus is mainly given to this condition, which is benchmarked against the Inconel 625 sample.

Fig. 5 a) and b) show the EBSD maps of the as-built Inconel 625 sample and that fabricated with 0.56 wt% TiB_2, respectively. In the as-built sample, the microstructure is mainly composed of columnar grains both in the remelted and non-remelted regions. With some of these continuously growing from one region to the other (epitaxial growth). Upon the addition of TiB_2 particles, fully equiaxed grains in the non-remelted regions are observed, and smaller dendrites both in size and width than the ones presented in the as-built sample (39.1 ± 4.3 vs 14.8 ± 2.5 μm, respectively). Besides the refinement effect during solidification providing heterogeneous nucleation sites ahead of the S/L interface in a supercooled zone, the introduction of TiB_2 substantially

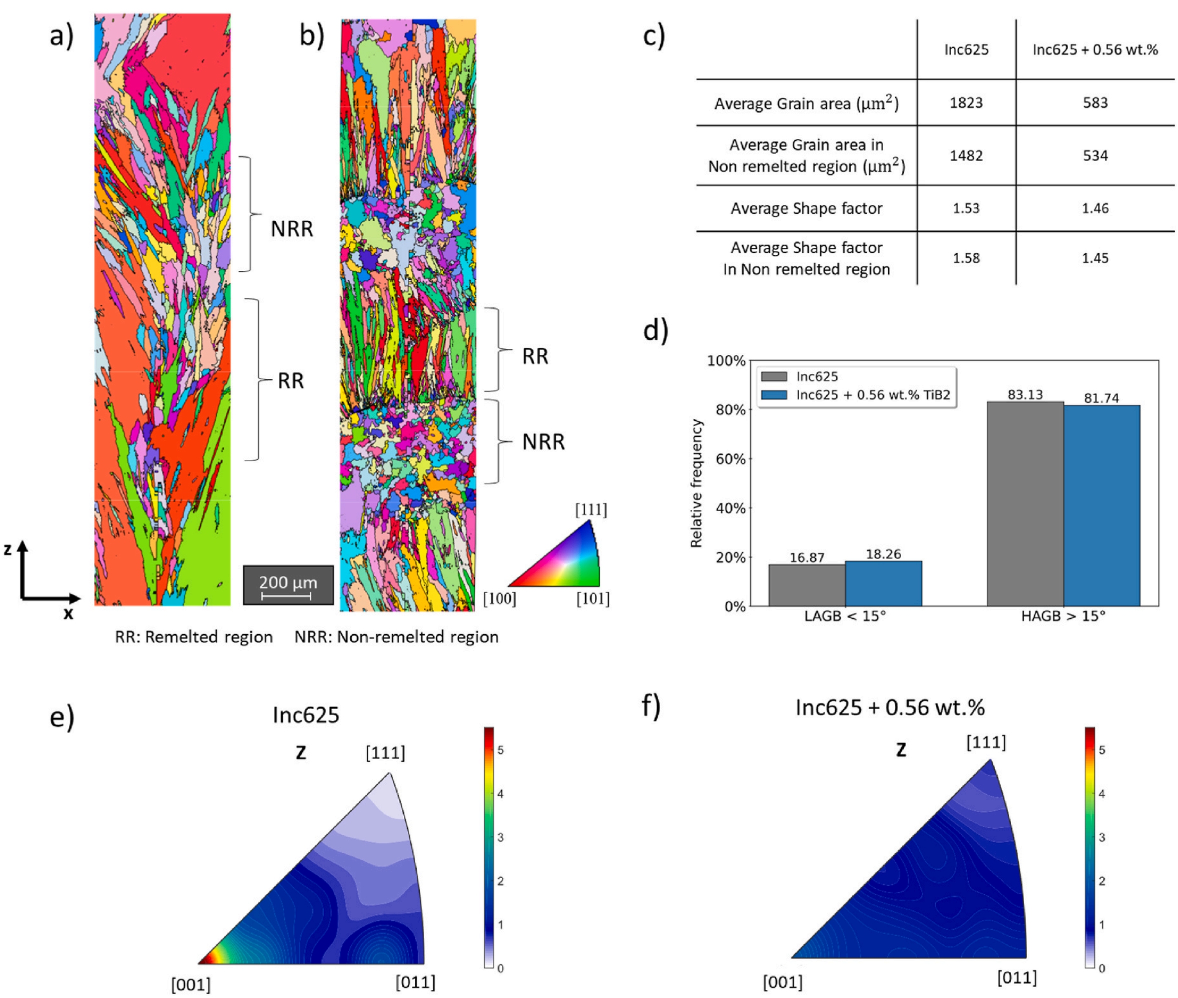

Fig. 5. – a) EBSD map of the as-built Inconel 625 sample; b) EBSD map of the Inconel 625 with 0.56 wt% TiB2; c) Grain shape parameters of the grains in the EBSD maps; d) Low and high grain boundaries angle density comparison; Comparison of inverse pole figures of texture for: e) as-built Inconel 625; f) Inconel 625 with 0.56 wt% TiB2.

refined the grain size including the width of the columnar grains. Thus, there is a positive synergetic effect of the TiB_2 particles: promote the columnar to equiaxed growth transition, while simultaneously increasing the nucleation sites for the next layer to solidify.

As in Fig. 5 c) the average grain area decreased from 1823 μm^2, in the as-built condition, to approximately 583 μm^2 for the TiB_2-containing sample. As a result of the refinement and equiaxed grains that formed with TiB_2, the average shape factor was reduced from 1.53 to 1.46, and in the non-remelted region from 1.58 to 1.45. The division between grain boundary types is based on the principle that for misorientation angles below 15°, these are referred to as low-angle grain boundaries (LAGBs), while for angles higher than 15° these are considered high-angle grain boundaries (HAGBs) [36]. Since grains come from the same formation mechanism (solidification), the number of LAGBs and HAGBs were similar between the samples.

In Fig. 5 e) it is found that grains in the as-built sample have a <001> preferential orientation which is parallel to the easy growth direction for metals with cubic structure, with the maximum density of grain orientation reaching 5.4. However, with the refinement of the microstructure upon the introduction of the TiB_2 particles, the microstructure became almost non-orientated, with the maximum density of grain orientation reaching only 2.2 (Fig. 5 f).

In the WAAM-fabricated Inconel 625 parts with the addition of TiB_2, each new layer has a mixture of columnar and equiaxed grains. This scenario is explained by the thermal gradients (G) that are not constant across the molten pool within a single deposited layer. Dynamically, there is a thermal gradient reduction from the bottom to the top of each layer [37]. During solidification ahead of the growing columnar dendrites, G is too high to allow nucleation from the dispersed particles. With further grain growth, G continues to decrease to a point where constitutional supercooling (ΔT_{CS}) equals or exceeds the temperature at which nucleation will occur (ΔT_N) and hence nucleation can occur from nearby particles. From this point on, the existing thermal gradients allow for constitutional supercooling to develop, triggering nucleation events within the supercooled zone from the dispersed TiB_2 particles [28,38]. The fact that the density of TiB_2 is smaller than that of liquid Inconel (7.39 vs 4.52 g/cm^3) [39], will also be beneficial to the heterogeneous nucleation as the particles of TiB_2 tend to be in the top regions of each layer [40] despite the intense convection motion in melting pool.

3.2. Synchrotron X-ray diffraction

Fig. 6 presents the synchrotron X-ray diffraction patterns for the fabricated samples. The as-built Inconel 625 presents γ, γ′, γ’’, Laves phase, and MC carbides. When TiB_2 is added to the molten pool of

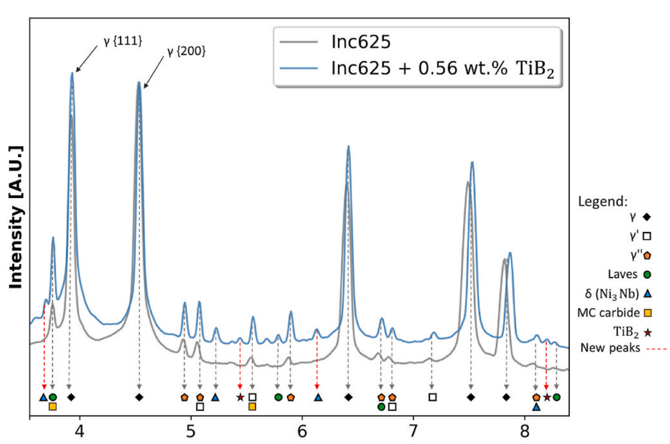

Fig. 6. *Synchrotron X-ray diffraction measurements for the WAAM fabricated parts with and without the introduction of TiB_2.*

Inconel, new diffraction peaks associated with the δ (Ni_3Nb) phase and TiB_2 are indexed. The formation of new peaks corresponding to the δ-phase suggests that partial dissolution of the TiB_2 occurred, as indicated by the Scheil-Gulliver solidification calculation for the modified alloy (refer to Fig. 4). This can reduce the potency of these inoculants to start nucleation due to the particle size reduction. The partial dissolution of TiB_2 resulted in an increase in Ti the remain liquid, which can induce a higher segregation of Ti to the interdendritic spaces during the solidification (partition coefficients lower than 1) [41]. It is stated in the literature that increasing the amount of Ti with respect to Al and Nb can improve the δ-phase nucleation kinetics along grain boundaries and high Nb-zones (e.g., around Laves phases), which can promote the δ-phase nucleation during the multiple reheating thermal cycles experienced by during part deposition [42,43]. Moreover, decreasing the Al/Ti ratio will also increase the mismatch between the γ matrix and γ′ precipitates, that further enhances the strength of the γ′ phase, but will also lower the thermal stability of the γ′ encouraging the precipitation of δ-phase [44–46]. The increased content of Ti in the matrix also presents some advantages as it contributes to restricting the dendrite growth of prior austenite grains [47] and consequently promoting heterogeneous nucleation ahead of the S/L interface. In addition, the increase of the intensity of the peak {111} (higher multiplicity factor) in relation to peak {200} for the Inc 625 + 0.56 wt % TiB_2 is a volumetric evidence (SXRD in transmission mode) of the effect of TiB_2 in refine the microstructure and reduce the texture aspects of the Inconel 625 fabricated by WAAM, which is in accordance with the EBSD results (Fig. 5).

To reinforce the SXDR data that TiB_2 particles were not completely dissolved/melted, a finite element model was developed to assess the maximum temperature of the melting pool (refer to Supplementary material). A good match exists between the temperatures simulated and those measured by thermocouples, as shown in Fig. 7 a, validated the heat source and the thermal boundaries conditions adopted in the model. The numerical simulation of 10 deposited layers (Fig. 7 b) calculated the maximum temperature that would develop inside the molten pool considering an interlayer temperature of 150 °C. The deposition strategy of regulating the next layer deposition based on the interlayer temperature showed that the maximum temperature of the molten pool was 2646 °C. After the 5th layer, the maximum temperature stabilized indicating a similar behavior when depositing any layer above this one, keeping the processing conditions constant. It is worth noting that the maximum temperature developed in the melt pool never reaches the melting temperature of TiB_2 (3225 °C), as showed in Fig. 7 b. These data reinforce the presence of TiB_2 particles on the melting pool, as also previously indicated by isolated diffractions peaks related to TiB_2 (Fig. 6). In addition, it is worth mentioning that the TiB_2 dissolution/melting can also occurred through the electric arc, which typically reach temperatures above melting temperature of TiB_2 (3225 °C) [48].

3.3. Mechanical properties

The average microhardness of the fabricated samples is depicted in Fig. 8. Hardness in the as-built sample is, on average, 228 HV, which is good agreement with the literature of WAAM of Inconel 625 which showed variations between 220 and 240 HV [49,50]. With a content of 0.31 wt% TiB_2, the increase in hardness was only 2 HV which is almost negligible. Only when the TiB_2 content increased to 0.56 wt% does a more notorious hardness increase to 238 HV occurs. As reported by Hu et al. [51] and Jena et al. [52], additions of Ti between 0 and 3 wt %, have an almost insignificant effect on the microhardness, indicating that, independently of the quantity of TiB_2 dissolved/melted, effect of solid solution strengthening of Ti on the microhardness is relatively small. Since the welding wire used in this study only has 0.4 wt% of Ti, adding 0.56 wt% of TiB_2 will not significantly affect the material hardness by solid solution strengthening, which reinforce the hypothesis that the main strengthening induced by the TiB_2 inoculants will be the grain size strengthening mechanisms.

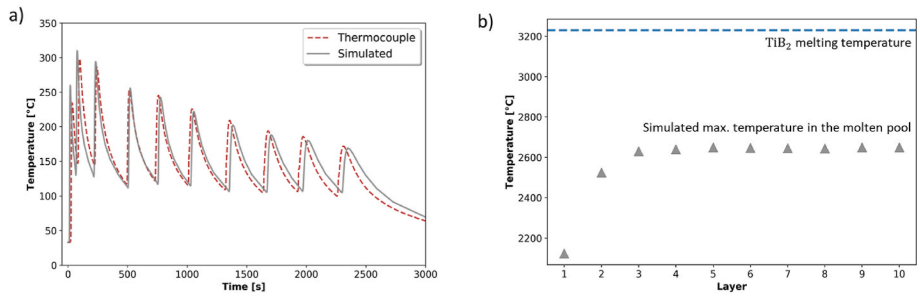

Fig. 7. a) Temperature simulated and measured by thermocouple during the deposition of the WAAM-fabricated wall; b) Estimation of the maximum temperature of the molten pool at each deposited layer.

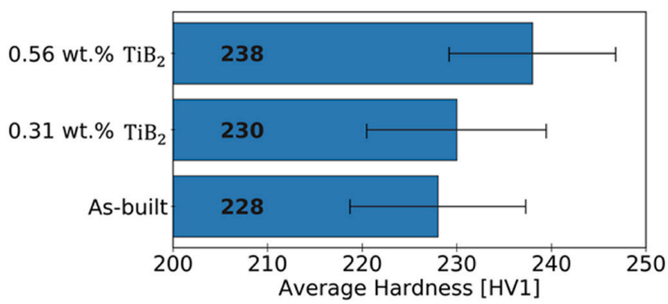

Fig. 8. Average microhardness measurements for the fabricated samples.

The average values of yield strength (σ_c) in the vertical and horizontal directions are shown in Fig. 9. In the literature, the values in yield strength in the vertical direction of Inconel 625 parts are between 373 MPa and 384 MPa, while in the horizontal direction the values reach approximately 380 MPa [50,53,54]. In Fig. 9, the yield strength of the as-built Inconel is 386 and 376 MPa in the horizontal and vertical directions, respectively. Therefore, it can be concluded that these values are within those expected for WAAMed Inconel 625. With the introduction of TiB_2 in a concentration of 0.56 wt%, the yield strength in the horizontal and vertical directions increased to 407 and 405 MPa, respectively. Moreover, the values between principal directions had only a difference of 2 MPa on average, while in the control sample the difference was 10 MPa. Thus, it can be concluded that the mechanical properties became more isotropic upon the introduction of TiB_2 particles. This isotropy can be directly correlated with the EBSD data (refer to Fig. 5), where the TiB_2 particles induced an almost-random texture since

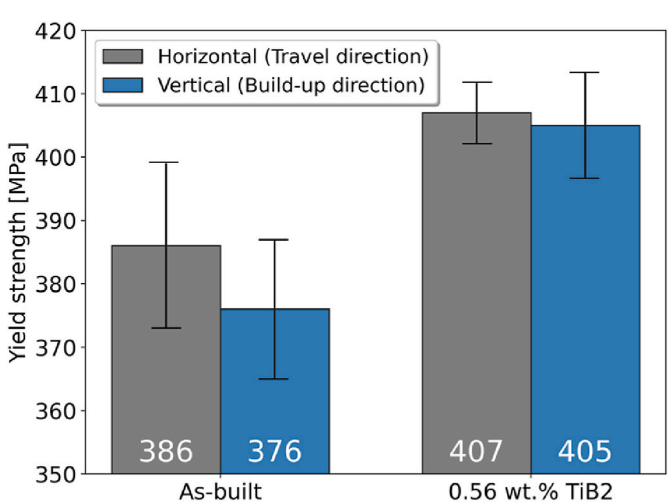

Fig. 9. Summary of yield strength obtained from compression tests taken both from the travel and build-up direction.

the columnar dendrites were replaced by mainly fine equiaxed grains in the non-remelted areas.

Gao et al. [36] studied the effect of the strengthening mechanisms (lattice friction stress, solid solution strengthening, grain boundary strengthening, twin boundary strengthening, and dislocation strengthening) on the yield strength of Inconel 625. Considering that both conditions (with and without the addition of TiB_2) underwent almost similar cooling rates, it is expected that the dislocation density will be similar for both conditions. In addition, as discussed in the previous paragraph, the solid solution strengthening was insignificantly affected by the inoculant; also, the material did not show twin structure (Fig. 5). In addition, Zhang et al. [55] reports that the strengthening mechanism of the interdendritic eutectics (MC-type carbides and Laves) is insignificant due to the low volume fraction and incoherent interface between the interdendritic eutectic and matrix, which can also be extended to remain TiB_2 particles. Thus, the major difference between Inconel 625 and Inconel 625 + 0.56 wt% TiB_2 will be the grain size (Fig. 5). The unique strengthening mechanism that remarkably varied between the analyzed conditions is the grain boundary strengthening, which can be estimated via the Hall–Petch relation $\left(\sigma_{gb} = \frac{\alpha}{D^{0.5}}\right)$ [56], where D is the grain size and α a constant ($750\ MPa \bullet \mu m^{-0.5}$). Therefore, considering the grain size measured via the intercept method (89.43 vs. 52.16 μm), the difference in σ_c for the as-built and 0.56 wt% TiB_2 condition was of ~24.5 MPa, which is in accordance with the experimental results depicted in Fig. 9 (increase of 21 and 29 MPa in the σ_c due to the addition of TiB_2). Additionally, Gao et al. [36] also reported that grain refinement was the factor that less contributed to the final strength of Inconel 625. These results allow explaining the moderate increase in yield strength observed in this work, around 5.4 % in the horizontal specimens and 7.7 % in the vertical specimens. However, the near isotropic properties are of major relevance, since these are typically preferred for structural applications subjected to multi-axial loadings. Thus, it can be concluded that the addition of TiB_2 during WAAM of Inconel 625 not only enhances the material's strength but also results in a finer and microstructure. This leads to near-isotropic properties in the fabricated parts due to grain size refinement and an almost non-oriented microstructure.

3.4. *Printing parameters and the role of inoculants*

Some remarks can be made regarding the use of inoculants and the process parameters design. A critical parameter for printing Ni-based alloys is the control of interpass temperature, which must be maintained within a narrow range, as indicated in the material datasheet or WPS. As demonstrate in Fig. 7, the temperature of the melting pool increases as the part is built and reaches a plateau; thus, if interpass temperature control is not performed, the temperature of the melting pool can rise, approaching the melting temperature of the inoculant particles, which may cause them to lose their effectiveness. Additionally, higher interpass temperatures reduce cooling time, meaning the time that the particles are in contact with the liquid metal increases (resulting in greater dissolution). Regarding printing velocity, it must be selected based on trial and test procedure, considering the bead geometry aspects and the presence of hot cracks. Furthermore, the wire feed speed is related to bead penetration. Thus, the selected wire feed speed must take into account bead penetration and the area of grain size refinement, ensuring that the refined area is larger than the penetration. This will enable a significant grain size refinement effect.

4. Conclusions

- A new feeding mechanism was developed to introduce particles (TiB_2) in the melting pool of single-bead multi-layer parts fabricated via gas metal arc-based additive manufacturing.
- Finite Element Method (FEM) simulations validated the deposition strategy, confirming that maintaining a constant interpass temperature would not lead to peak temperatures in the molten pool exceeding the melting point of TiB_2.
- TiB_2 added particles reduce the interdendritic segregation and the grain size. A minor TiB_2 content (0.56 wt%) was sufficient to transform columnar grains into equiaxed grains for Inconel 625 fabricated by WAAM. The average grain area exhibited a substantial reduction from 1823 μm^2 in the as-built sample to 583 μm^2 in the sample with 0.56 wt% TiB_2 content.
- The introduction of 0.56 wt% TiB_2 particles led to an enhancement in material yield strength (from 386 to 407 MPa in the horizontal direction and from 376 to 405 MPa in the build-up direction) and hardness (from 228 to 238 HV). Thus, the introduction of TiB_2 particles promotes an isotropic material.

The impact of introducing TiB_2 depending on whether the particles dissolve or not. In cases of dissolution, the content of Ti and B in the molten pool will increase, which can promote the formation of δ-phase. When particles were not fully dissolve, TiB_2 act as inoculant within the constitutional supercooled zone, generating equiaxed grains and refining the unavoidable columnar grains. This multifaceted study highlights the potential for tailoring microstructures and mechanical properties in WAAM-fabricated components through the incorporation of TiB_2 particles.

CRediT authorship contribution statement

Tiago A. Rodrigues: Writing – original draft, Investigation, Formal analysis. **A. Malfeito:** Investigation. **Francisco Werley Cipriano Farias:** Investigation, Formal analysis. **V. Duarte:** Investigation. **João Lopes:** Investigation. **João da Cruz Payão Filho:** Investigation. **Julian A. Avila:** Investigation. **N. Schell:** Investigation. **Telmo G. Santos:** Writing – review & editing, Validation, Methodology, Formal analysis. **J.P. Oliveira:** Writing – review & editing, Supervision, Methodology, Investigation, Formal analysis, Conceptualization.

Declaration of competing interest

The authors declare the following financial interests/personal relationships which may be considered as potential competing interests:

Tiago Rodrigues, Valdemar Duarte, Telmo Santos and Joao Pedro Oliveira have patent pending.

5. Acknowledgments

TAR acknowledges FCT – MCTES for funding the Ph.D. grant SFRH/BD/144202/2019. TAR, AM, FF, TGS, and JPO acknowledge Fundação para a Ciência e a Tecnologia (FCT – MCTES) for its financial support via the project UID/00667/2020 (UNIDEMI). JPO acknowledges funding by national funds from FCT - Fundação para a Ciência e a Tecnologia, I.P., in the scope of the projects LA/P/0037/2020, UIDP/50025/2020 and UIDB/50025/2020 of the Associate Laboratory Institute of Nanostructures, Nanomodelling and Nanofabrication – i3N. This activity has received funding from the European Institute of Innovation and Technology (EIT) – Project Smart WAAM: Microstructural Engineering and Integrated Non-Destructive Testing. This body of the European Union receives support from the European Union's Horizon 2020 research and innovation program. FWCF acknowledges Fundação para a Ciência e a Tecnologia (FCT-MCTES) for funding the Ph.D. Grant 2022.13870.BD. J. Avila is a fellow from CNPq under grant 306960/2021-4.

Appendix A. Supplementary data

Supplementary data to this article can be found online at https://doi.org/10.1016/j.intermet.2024.108540.

Data availability

Data will be made available on request.

References

[1] ASTM F3187-16, Standard Guide for Directed Energy Deposition of Metals, n.d.
[2] F. Martina, J. Ding, S. Williams, A. Caballero, G. Pardal, L. Quintino, Tandem metal inert gas process for high productivity wire arc additive manufacturing in stainless steel, Addit. Manuf. (2018), https://doi.org/10.1016/j.addma.2018.11.022.
[3] S.W. Williams, F. Martina, A.C. Addison, J. Ding, G. Pardal, P. Colegrove, Wire + Arc additive manufacturing, Mater. Sci. Technol. 32 (2016) 641–647, https://doi.org/10.1179/1743284715Y.0000000073.
[4] T.A. Rodrigues, F.W. Cipriano Farias, J.A. Avila, E. Maawad, N. Schell, T.G. Santos, J.P. Oliveira, Effect of heat treatments on Inconel 625 fabricated by wire and arc additive manufacturing: an in situ synchrotron X-ray diffraction analysis, Sci. Technol. Weld. Join. (2023), https://doi.org/10.1080/13621718.2023.2187927.
[5] F.W.C. Farias, V.R. Duarte, I.O. Felice, J. da C.P. Filho, N. Schell, E. Maawad, J. Y. Li, Y. Zhang, T.G. Santos, J.P. Oliveira, In situ interlayer hot forging arc plasma directed energy deposition of Inconel® 625: microstructure evolution during heat treatments, J. Alloys Compd. 952 (2023), https://doi.org/10.1016/j.jallcom.2023.170059.
[6] F.W.C. Farias, V.R. Duarte, I.O. Felice, J. da C.P. Filho, N. Schell, E. Maawad, J. A. Avila, J.Y. Li, Y. Zhang, T.G. Santos, J.P. Oliveira, In situ interlayer hot forging arc-based directed energy deposition of Inconel® 625: process development and microstructure effects, Addit. Manuf. 66 (2023), https://doi.org/10.1016/j.addma.2023.103476.
[7] H. Li, Y. Huang, S. Jiang, Y. Lu, X. Gao, X. Lu, Z. Ning, J. Sun, Columnar to equiaxed transition in additively manufactured CoCrFeMnNi high entropy alloy, Mater. Des. 197 (2021) 109262, https://doi.org/10.1016/j.matdes.2020.109262.
[8] R.A. Michi, A. Plotkowski, A. Shyam, R.R. Dehoff, S.S. Babu, Towards high-temperature applications of aluminium alloys enabled by additive manufacturing, Int. Mater. Rev. 67 (2022) 298–345, https://doi.org/10.1080/09506608.2021.1951580.
[9] J.A. Spittle, Columnar to equiaxed grain transition in as solidified alloys, Int. Mater. Rev. 51 (2006) 247–269, https://doi.org/10.1179/174328006X102493.
[10] W. Kurz, C. Bezençon, M. Gäumann, Columnar to equiaxed transition in solidification processing, Sci. Technol. Adv. Mater. 2 (2001) 185–191, https://doi.org/10.1016/S1468-6996(01)00047-X.
[11] R.M. Kindermann, M.J. Roy, R. Morana, P.B. Prangnell, Process response of Inconel 718 to wire + arc additive manufacturing with cold metal transfer, Mater. Des. 195 (2020), https://doi.org/10.1016/j.matdes.2020.109031.
[12] M.J. Bermingham, D.H. StJohn, J. Krynen, S. Tedman-Jones, M.S. Dargusch, Promoting the columnar to equiaxed transition and grain refinement of titanium alloys during additive manufacturing, Acta Mater. 168 (2019) 261–274, https://doi.org/10.1016/j.actamat.2019.02.020.
[13] T.A. Rodrigues, V.R. Duarte, D. Tomás, J.A. Avila, J.D. Escobar, E. Rossinyol, N. Schell, T.G. Santos, J.P. Oliveira, In-situ strengthening of a high strength low alloy steel during Wire and Arc Additive Manufacturing (WAAM), Addit. Manuf. 34 (2020) 101200, https://doi.org/10.1016/j.addma.2020.101200.
[14] F.W.C. Farias, J. da C. Payão Filho, V.H.P. Moraes e Oliveira, Prediction of the interpass temperature of a wire arc additive manufactured wall: FEM simulations and artificial neural network, Addit. Manuf. 48 (2021) 102387, https://doi.org/10.1016/j.addma.2021.102387.
[15] B. Wu, Z. Pan, D. Ding, D. Cuiuri, H. Li, Z. Fei, The effects of forced interpass cooling on the material properties of wire arc additively manufactured Ti6Al4V alloy, J. Mater. Process. Technol. 258 (2018) 97–105, https://doi.org/10.1016/j.jmatprotec.2018.03.024.
[16] V.R. Duarte, T.A. Rodrigues, N. Schell, R.M. Miranda, J.P. Oliveira, T.G. Santos, Hot forging wire and arc additive manufacturing (HF-WAAM), Addit. Manuf. 35 (2020) 101193, https://doi.org/10.1016/j.addma.2020.101193.
[17] A.R. McAndrew, M. Alvarez Rosales, P.A. Colegrove, J.R. Hönnige, A. Ho, R. Fayolle, K. Eyitayo, I. Stan, P. Sukrongpang, A. Crochemore, Z. Pinter, Interpass rolling of Ti-6Al-4V wire + arc additively manufactured features for

microstructural refinement, Addit. Manuf. 21 (2018) 340–349, https://doi.org/10.1016/j.addma.2018.03.006.
[18] C.J. Todaro, M.A. Easton, D. Qiu, D. Zhang, M.J. Bermingham, E.W. Lui, M. Brandt, D.H. StJohn, M. Qian, Grain structure control during metal 3D printing by high-intensity ultrasound, Nat. Commun. 11 (2020) 1–9, https://doi.org/10.1038/s41467-019-13874-z.
[19] M.J. Bermingham, D. Kent, H. Zhan, D.H. Stjohn, M.S. Dargusch, Controlling the microstructure and properties of wire arc additive manufactured Ti-6Al-4V with trace boron additions, Acta Mater. 91 (2015) 289–303, https://doi.org/10.1016/j.actamat.2015.03.035.
[20] A. Prasad, L. Yuan, P.D. Lee, D.H. Stjohn, The Interdependence model of grain nucleation: a numerical analysis of the Nucleation-Free Zone, Acta Mater. 61 (2013) 5914–5927, https://doi.org/10.1016/j.actamat.2013.06.015.
[21] S. Mereddy, M.J. Bermingham, D.H. StJohn, M.S. Dargusch, Grain refinement of wire arc additively manufactured titanium by the addition of silicon, J. Alloys Compd. 695 (2017) 2097–2103, https://doi.org/10.1016/j.jallcom.2016.11.049.
[22] A. Joseph, D. Harwig, D.F. Farson, R. Richardson, Measurement and calculation of arc power and heat transfer efficiency in pulsed gas metal arc welding, Sci. Technol. Weld. Join. 8 (2003) 400–406, https://doi.org/10.1179/136217103225005642.
[23] B. Basu, G.B. Raju, A.K. Suri, Processing and properties of monolithic TiB2 based materials, Int. Mater. Rev. 51 (2006) 352–374, https://doi.org/10.1179/174328006X102529.
[24] L. Xu, C. Cui, X. Sun, The effects of Co and Ti additions on microstructures and compressive strength of Udimet710, Mater. Sci. Eng. 528 (2011) 7851–7856, https://doi.org/10.1016/j.msea.2011.07.019.
[25] B. Tang, Y. Tan, T. Xu, Z. Sun, X. Li, Ni-Based Composite Coatings Reinforced with TiB 2, 2020.
[26] B. Zhang, G. Bi, P. Wang, J. Bai, Y. Chew, M.S. Nai, Microstructure and mechanical properties of Inconel 625/nano-TiB2 composite fabricated by LAAM, Mater. Des. 111 (2016) 70–79, https://doi.org/10.1016/j.matdes.2016.08.078.
[27] M.J. Bermingham, S.D. McDonald, M.S. Dargusch, Effect of trace lanthanum hexaboride and boron additions on microstructure, tensile properties and anisotropy of Ti-6Al-4V produced by additive manufacturing, Mater. Sci. Eng. 719 (2018) 1–11, https://doi.org/10.1016/j.msea.2018.02.012.
[28] M.J. Bermingham, D.H. StJohn, J. Krynen, S. Tedman-Jones, M.S. Dargusch, Promoting the columnar to equiaxed transition and grain refinement of titanium alloys during additive manufacturing, Acta Mater. 168 (2019) 261–274, https://doi.org/10.1016/j.actamat.2019.02.020.
[29] A.N. F, D.H.A.P. Hammersley, S.O. Svensson, M. Hanfland, Two-dimensional detector software: from real detector to idealised image or two-theta scan, High Press Res. 14 (1996) 4–6, https://doi.org/10.1080/08957959608201408, 235–248.
[30] ASTM Standard E9-09, Standard Test Methods of Compression Testing of Metallic Materials at Room Temperature, 2012, https://doi.org/10.1520/E0009-09.2 n.d.
[31] J. Goldak, A. Chakravarti, M. Bibby, A new finite element model for welding heat sources, Metall. Trans. A B 15 (1984) 299–305, https://doi.org/10.1007/BF02667333.
[32] X. Wang, P.W. Liu, Y. Ji, Y. Liu, M.H. Horstemeyer, L. Chen, Investigation on microsegregation of IN718 alloy during additive manufacturing via integrated phase-field and finite-element modeling, J. Mater. Eng. Perform. 28 (2019) 657–665, https://doi.org/10.1007/s11665-018-3620-3.
[33] S. Sui, H. Tan, J. Chen, C. Zhong, Z. Li, W. Fan, A. Gasser, W. Huang, The influence of Laves phases on the room temperature tensile properties of Inconel 718 fabricated by powder feeding laser additive manufacturing, Acta Mater. 164 (2019) 413–427, https://doi.org/10.1016/j.actamat.2018.10.032.
[34] G. Blaine, L. Hugo, H. Xiao, Superalloys: Alloying and Performance, 1°, AMS International, 2010 https://doi.org/10.31399/asm.tb.sap.9781627083133.
[35] J. Näkki, J. Tuominen, P. Vuoristo, Effect of minor elements on solidification cracking and dilution of alloy 625 powders in laser cladding, J. Laser Appl. 29 (2017) 012014, https://doi.org/10.2351/1.4973673.
[36] Y. Gao, Y. Ding, J. Chen, J. Xu, Y. Ma, X. Wang, Effect of twin boundaries on the microstructure and mechanical properties of Inconel 625 alloy, Materials Science and Engineering: A 767 (2019) 138361, https://doi.org/10.1016/j.msea.2019.138361.
[37] H. Li, Y. Huang, S. Jiang, Y. Lu, X. Gao, X. Lu, Z. Ning, J. Sun, Columnar to equiaxed transition in additively manufactured CoCrFeMnNi high entropy alloy, Mater. Des. 197 (2021) 109262, https://doi.org/10.1016/j.matdes.2020.109262.
[38] D.H. StJohn, A. Prasad, M.A. Easton, M. Qian, The contribution of constitutional supercooling to nucleation and grain formation, Metall Mater Trans A Phys Metall Mater Sci 46 (2015) 4868–4885, https://doi.org/10.1007/s11661-015-2960-y.
[39] H.P. Wang, C.H. Zheng, P.F. Zou, S.J. Yang, L. Hu, B. Wei, Density determination and simulation of Inconel 718 alloy at normal and metastable liquid states, J. Mater. Sci. Technol. 34 (2018) 436–439, https://doi.org/10.1016/j.jmst.2017.10.014.
[40] Z.S., X.L. Binghui Tang, Yefa Tan, Zhongwei Zhang, Ting Xu, Effects of process parameters on geometrical characteristics, microstructure and tribological properties of TiB2 reinforced inconel 718 alloy composite coatings by laser cladding, Coatings (2020) 3–8.
[41] M. Solecka, A. Kopia, A. Radziszewska, B. Rutkowski, Microstructure, microsegregation and nanohardness of CMT clad layers of Ni-base alloy on 16Mo3 steel, J. Alloys Compd. 751 (2018) 86–95, https://doi.org/10.1016/j.jallcom.2018.04.102.
[42] W.-D. Cao, R. Kennedy, Role of Chemistry in 718-type Alloys - ALLVAC 718PLUS Alloy Development, vol. 3, 2004, pp. 1–10.
[43] J. Jang, D. Van, S.H. Lee, Precipitation kinetics of secondary phases induced by heat accumulation in the deposit of Inconel 718, Addit. Manuf. 55 (2022) 102831, https://doi.org/10.1016/J.ADDMA.2022.102831.
[44] J.P. Collier, S.H. Wong, J.K. Tien, J.C. Phillips, J.K. Tein, EFFECT OF VARYING Al, Ti, AND Nb CONTENT ON THE PHASE STABILITY OF INCONEL 718, Metall. Trans. A 19 A (1988) 1657–1666, https://doi.org/10.1007/bf02645133.
[45] B. Hassan, J. Corney, Grain boundary precipitation in Inconel 718 and ATI 718Plus, Mater. Sci. Technol. 33 (2017) 1879–1889, https://doi.org/10.1080/02670836.2017.1333222.
[46] W.-D. Cao, R. Kennedy, Role of Chemistry in 718-type Alloys - ALLVAC 718PLUS Alloy Development, vol. 3, 2004, pp. 1–10.
[47] S.Y. Seo, S.J. Lee, Effects of Ti and Nb on the grain refinement and mechanical properties of AISI 4145 steel, Trans. Indian Inst. Met. 71 (2018) 3037–3043, https://doi.org/10.1007/s12666-018-1405-x.
[48] S. Cadiou, M. Courtois, M. Carin, W. Berckmans, P. Le masson, 3D heat transfer, fluid flow and electromagnetic model for cold metal transfer wire arc additive manufacturing (Cmt-Waam), Addit. Manuf. 36 (2020) 101541, https://doi.org/10.1016/J.ADDMA.2020.101541.
[49] A.N.M. Tanvir, M.R.U. Ahsan, G. Seo, J. duk Kim, C. Ji, B. Bates, Y. Lee, D.B. Kim, Heat treatment effects on Inconel 625 components fabricated by wire + arc additively manufacturing (WAAM)—part 2: mechanical properties, Int. J. Adv. Manuf. Technol. 110 (2020) 1709–1721, https://doi.org/10.1007/s00170-020-05980-w.
[50] Y. Wang, X. Chen, Q. Shen, C. Su, Y. Zhang, S. Jayalakshmi, R.A. Singh, Effect of magnetic Field on the microstructure and mechanical properties of inconel 625 superalloy fabricated by wire arc additive manufacturing, J. Manuf. Process. 64 (2021) 10–19, https://doi.org/10.1016/j.jmapro.2021.01.008.
[51] Y.L. Hu, X. Lin, X.B. Yu, J.J. Xu, M. Lei, W.D. Huang, Effect of Ti addition on cracking and microhardness of Inconel 625 during the laser solid forming processing, J. Alloys Compd. 711 (2017) 267–277, https://doi.org/10.1016/j.jallcom.2017.03.355.
[52] A.K. Jena, M.C. Chaturvedi, The role of alloying elements in the design of nickel-base superalloys, J. Mater. Sci. 19 (1984) 3121–3139, https://doi.org/10.1007/BF00549796.
[53] A.N.M. Tanvir, M.R.U. Ahsan, C. Ji, W. Hawkins, B. Bates, Duck, B. Kim, Heat treatment effects on Inconel 625 components fabricated by wire + arc additive manufacturing (WAAM)-part 1: microstructural characterization, Int. J. Adv. Des. Manuf. Technol. 103 (2019) 3785–3798, https://doi.org/10.1007/s00170-019-03828-6.
[54] W. Yangfan, C. Xizhang, S. Chuanchu, Microstructure and mechanical properties of Inconel 625 fabricated by wire-arc additive manufacturing, Surf. Coat. Technol. 374 (2019) 116–123, https://doi.org/10.1016/j.surfcoat.2019.05.079.
[55] S. Zhang, X. Lin, L. Wang, X. Yu, Y. Hu, H. Yang, L. Lei, W. Huang, Strengthening mechanisms in selective laser-melted Inconel718 superalloy, Materials Science and Engineering: A. 812 (2021), https://doi.org/10.1016/j.msea.2021.141145.